Sparsity-Constrained Coupled Nonnegative Matrix–Tensor Factorization for Hyperspectral Unmixing

Heng-Chao Li, *Senior Member, IEEE*, Shuang Liu, Xin-Ru Feng, and Shao-Quan Zhang

***Abstract*—Hyperspectral unmixing refers to a source separation problem of decomposing a hyperspectral imagery (HSI) to estimate endmembers, and their corresponding abundances. Recently, matrix–vector nonnegative tensor factorization (MV-NTF) was proposed for unmixing to avoid structure information loss, which is caused by the HSI cube unfolding in nonnegative matrix factorization (NMF)-based methods. However, MV-NTF ignores local spatial information due to directly dealing with data as a whole, meanwhile, the forceful rank constraint in low-rank tensor decomposition loses some detailed structures. Unlike MV-NTF works at the original data, the pixel-based NMF is more adaptive to learn local spatial variations. Hence, from the perspective of multi-view, it is significant to utilize the complementary advantages of MV-NTF and NMF to fully preserve the intrinsic structure information, and exploit more detailed spatial information. In this article, we propose a sparsity-constrained coupled nonnegative matrix-tensor factorization (SCNMTF) model for unmixing, wherein MV-NTF and NMF are subtly coupled by sharing endmembers and abundances. Since the representations for abundances in MV-NTF and NMF are distinct, abundance sharing is achieved indirectly by introducing an auxiliary constraint. Furthermore, the $L_{1/2}$ regularizer is adopted to promote the sparsity of abundances. A series of experiments on synthetic and real hyperspectral data demonstrate the effectiveness of the proposed SCNMTF method.**

***Index Terms*—Coupled decomposition, hyperspectral unmixing, nonnegative matrix factorization (NMF), nonnegative tensor factorization (NTF), sparsity constraint.**

I. Introduction

HYPERSPECTRAL imagery (HSI) contains a range of spectra from ultraviolet to infrared bands, providing affluent information to detect and identify ground objects. Therefore, HSI advances active research in various fields: classification [1], object detection [2], and data fusion [3], etc. Due to the limited spatial resolution of spectrometer, diverse materials present in the scene, and multiple scattering, the spectrum of an observed pixel is generally a combination of these spectra of several materials, resulting in mixed pixel. The prevalence of mixed pixel has a negative impact on the follow-up analysis for hyperspectral data. Hence, hyperspectral unmixing offers a possible solution. Given an observed mixed pixel, unmixing aims at estimating the individual materials involved (named as endmembers) and their corresponding fractional proportions (named as abundances), which actually is a source separation problem [4].

Linear mixture model (LMM) assumes the spectrum of each pixel is a linear mixture of all endmember spectra associated with their abundances [4], which is the basis of many classical unmixing algorithms. Geometry-based methods conjecture that endmembers correspond to the vertices of a simplex formed by a HSI in the feature space, whose representative methods include independent component analysis (ICA) [5], N-FINDR [6], vertex component analysis (VCA) [7], and minimum volume simplex analysis (MVSA) [8]. However, this category focuses on extracting endmembers, thus needs to further combine with abundance estimation algorithms, such as fully constrained least squares (FCLS) [9]. Another kind of unmixing methods is based on sparse regression, where a spectral library is used to replace the endmember set [10]–[12].

Hyperspectral unmixing can be seen as a blind source separation (BSS), which simultaneously estimates the endmembers and the abundances from a statistical perspective [13]–[15]. Among them, nonnegative matrix factorization (NMF) [16]–[19] has drawn much attention owing to its nonnegativity, less prior requirements, and desirable performance. NMF decomposes a given HSI data into two nonnegative matrices, representing endmembers and abundances, respectively. The model nonconvexity of NMF usually leads to a local optimal solution. Consequently, a variety of constraints have been added to improve unmixing performance [20]–[24]. Nevertheless, the loss of spatial information and potential correlation between different dimensions is inevitable when a 3-D HSI data is unfolded into a 2-D matrix. In order to make up for the information loss, various assumptions and constraints have been integrated into NMF. For instance, methods in [25] and [26] added total variation (TV) constraint on abundance maps to promote piecewise smoothness. The graph-regularized $L_{1/2}$-NMF was proposed by embedding manifold structure [27]. Wang *et al.* [28] added semantic information to exploit spectral-spatial joint structure.

Manuscript received June 5, 2020; revised August 2, 2020; accepted August 19, 2020. Date of publication August 26, 2020; date of current version September 16, 2020. This work was supported in part by the National Natural Science Foundation of China under Grant 61871335 and Grant 61901208, in part by the Fundamental Research Funds for the Central Universities under Grant 2682020XG02 and Grant 2682020ZT35, and in part by the Jiangxi Provincial Natural Science Foundation under Grant 20192BAB217003. *(Corresponding author: Heng-Chao Li.)*

Heng-Chao Li, Shuang Liu, and Xin-Ru Feng are with the School of Information Science, and Technology, Southwest Jiaotong University, Chengdu 610031, China (e-mail: lihengchao_78@163.com; liushuangtcl@163.com; fengxinru@my.swjtu.edu.cn).

Shao-Quan Zhang is with the Jiangxi Province Key Laboratory of Water Information Cooperative Sensing and Intelligent Processing, Nanchang Institute of Technology, Nanchang 330099, China (e-mail: zhangshaoquan1@163.com).

Digital Object Identifier 10.1109/JSTARS.2020.3019706

Nonetheless, these methods compensate information loss in an indirect way and still cannot fully preserve HSI structures.

As the high-dimensional extension of matrix, a third-order tensor is more suitable for HSI data cube, which has been widely used in data compression [29], feature extraction [30], and denoising [31]. In order to effectively preserve the intrinsic information of HSI, nonnegative tensor factorization (NTF) was first applied to unmixing by using canonical polyadic decomposition (CPD) in [32] and [33]. However, these traditional tensor factorization methods, like CPD and Tucker decomposition [32]–[35], lack an explicit link with LMM and physical interpretation. Recently, Qian *et al.* [36] proposed a matrix–vector NTF (MV-NTF) unmixing method, which was the first to construct a straightforward link between LMM and tensor factorization. MV-NTF is a low-rank tensor decomposition based on block term decomposition (BTD) [37], where a HSI tensor is decomposed into a sum of component tensors, and each of which is treated as an outer product of a matrix and a vector, representing abundances and endmember, respectively. The experimental result in [36] shows that MV-NTF outperforms some state-of-the-art NMF-based unmixing methods in most cases. Similar to NMF, three constraints were integrated into MV-NTF in [38], including sparseness, minimum volume, and robust nonlinearity. Xiong *et al.* [39] incorporated TV regularization on abundance maps.

MV-NTF works in the high-dimensional tensor space, and can avoid the loss of original structure information caused by data unfolding in NMF. Unfortunately, the local spatial information is not fully exploited in MV-NTF. This may be caused by the strict rank constraint in low-rank tensor decomposition, which cannot adequately capture small variations. In addition, MV-NTF is more concerned with global structures but ignores local spatial structures when directly deals with data as a whole. As a consequence, the abundance maps estimated by MV-NTF are more likely to lose small-scale details and be oversmoothing. On the contrary, NMF works in the vector space, and does not require compulsory consideration of contextual information through dealing with HSI at the pixel level, which can characterize more local spatial details. Hence, there is a complementarity between MV-NTF and NMF, as demonstrated in Section III-A.

From the perspective of multi-view, it is significant to integrate NMF into MV-NTF model to make full use of their individual advantages. Therefore, in this article, MV-NTF and NMF are coupled with each other by artfully sharing endmembers and abundances to retrain the intrinsic structure information of HSI data and exploit more detailed spatial information. It is noteworthy that, this coupled scheme is explored in two different dimensional spaces, which differs from the coupled matrix (or tensor) factorization based on the same dimensional space in HSI fusion [40], [41]. Specifically, the given HSI data in our proposed method is simultaneously represented as a third-order tensor for MV-NTF and unfolded into a matrix for NMF. Since the representations for abundances in these two decompositions are distinct, the abundance sharing cannot be achieved simply by using the same abundance variable. To tackle this problem, an auxiliary constraint is introduced to impose these two abundances equal. Moreover, when one of the abundance variables is optimized, the representation for the other one in the abundance sharing constraint is transformed into the same as it to facilitate optimization.

In this article, a new hyperspectral unmixing method called sparsity-constrained coupled nonnegative matrix-tensor factorization (SCNMTF) is proposed, which is proven to be effective with the benefits of the coupled model and the sparsity of abundances. The major contributions of our proposed SCNMTF method are given as follows.

1) To take the advantages of decompositions over different dimensional spaces from multi-view, it is the first attempt to incorporate NMF into MV-NTF by coupling, which can retain the original structure information by MV-NTF and characterize more local spatial details by the pixel-based NMF. In addition, the $L_{1/2}$ regularizer is adopted to promote the sparsity of abundance matrix by exploiting the fact that most pixels are mixed only by a few of endmembers.
2) Due to the representations for two abundances in different dimensional decompositions are distinct, abundance sharing cannot be achieved by directly using the same abundance variable, but by introducing an auxiliary constraint. Besides, in order to simplify optimization, the representation for one of the abundance variables in the constraint is transformed into the same as the other one currently being optimized.
3) From the mathematical perspective, such coupling can be seen as an implicit constraint to further reduce the solution space and enhance stability. Furthermore, the coupled model can avoid sensitive parameters introduced by extra constraints. Experimental results on synthetic and real hyperspectral data illustrate the advantage of our proposed SCNMTF method.

The rest of this article is organized as follows. Section II introduces previous work related to spectral unmixing. Section III presents the proposed SCNMTF model, as well as its solution estimation process and update rules. A series of experiments are conducted in Section IV. Finally, Section V draws the conclusion and discusses future work.

II. Related Work

A. Concepts and Operations

Some notations and concepts of multilinear algebra involved in latter work are introduced here. Euler script letter represents tensor, e.g., $\mathcal{Y}$; a matrix is a second-order tensor denoted by boldface capital letter, e.g., $\mathbf{Y}$; a vector is a first-order tensor denoted by bold lowercase letter, e.g., $\mathbf{y}$; a scalar is a tensor of order zero denoted by lowercase letter, e.g., y.

Definition 1: A Nth-order tensor $\mathcal{Y} \in \mathbb{R}^{I_1 \times \cdots \times I_N}$ can be unfolded into matrix from different mode-n ($1 \leq n \leq N$). The entries of matrix $\mathbf{Y}_{(k)} \in \mathbb{R}^{I_1 \cdots I_{k-1} I_{k+1} \cdots I_N \times I_k}$ unfolded from mode-k are given as

$$\mathbf{Y}_{(k)}(\overline{i_1 \cdots i_{k-1} i_{k+1} \cdots i_N}, i_k) = y_{i_1 i_2 \cdots i_N} \tag{1}$$

where $\overline{i_1 \cdots i_{k-1} i_{k+1} \cdots i_N}$ is the multi-index, and defined as $\overline{i_1 \cdots i_{k-1} i_{k+1} \cdots i_N} = i_1 + (i_2 - 1)I_1 + (i_3 - 1)I_1 I_2 + \cdots + (i_N - 1)I_1 \cdots I_{N-1}$ for $i_n = 1, 2, \ldots, I_n, n = 1, 2, \ldots, N$.

Definition 2 : Let $\otimes$ denotes the Kronecker product, the Khatri–Rao product of two matrices $\mathbf{A} \in \mathbb{R}^{I \times J}$ and $\mathbf{B} \in \mathbb{R}^{P \times J}$ with the same number of columns J is defined as

$$\mathbf{A} \odot \mathbf{B} = (\mathbf{a}_1 \otimes \mathbf{b}_1 \ \cdots \ \mathbf{a}_J \otimes \mathbf{b}_J). \tag{2}$$

Definition 3 : Given $\mathbf{A} = [\mathbf{A}_1 \cdots \mathbf{A}_R]$ and $\mathbf{B} = [\mathbf{B}_1 \cdots \mathbf{B}_R]$ with the same number of submatrices, their generalized Khatri–Rao product is defined as

$$\mathbf{A} \bar{\odot} \mathbf{B} = (\mathbf{A}_1 \otimes \mathbf{B}_1 \ \cdots \ \mathbf{A}_R \otimes \mathbf{B}_R). \tag{3}$$

B. Linear Mixture Model

The LMM assumes that the spectrum of a mixed pixel is a linear mixture of these spectra of all endmembers. $\mathbf{Y} := [\mathbf{y}_1, \mathbf{y}_2, \ldots, \mathbf{y}_P] \in \mathbb{R}^{K \times P}$ denotes the observed data with P pixels and K spectral bands, in which $\mathbf{y}_i$ represents the signature corresponding to the ith mixed pixel in HSI. $\mathbf{C} := [\mathbf{c}_1, \mathbf{c}_2, \ldots, \mathbf{c}_R] \in \mathbb{R}^{K \times R}$ refers to endmember matrix with R endmembers. Abundance matrix $\mathbf{S} := [\mathbf{s}_1, \mathbf{s}_2, \ldots, \mathbf{s}_P] \in \mathbb{R}^{R \times P}$ refers to the corresponding proportions of all endmembers in each pixel. Then, LMM can be formulated as

$$\mathbf{Y} = \mathbf{CS} + \mathbf{N} \tag{4}$$

where $\mathbf{N} \in \mathbb{R}^{K \times P}$ denotes the noise matrix.

Generally, all components in $\mathbf{C}$ and $\mathbf{S}$ should be nonnegative under the physical mechanism. Besides, the sum of entries in each $\mathbf{s}_i$ should be equal to one. The abundance sum-to-one constraint (ASC) can be expressed as

$$\mathbf{1}_R^T \mathbf{S} = \mathbf{1}_P^T. \tag{5}$$

C. Matrix–Vector Nonnegative Tensor Factorization

MV-NTF is a special case of BTD, and whose solution is hard to be unique unless rigorous conditions are met [42], [43]. MV-NTF decomposes an original third-order data into a sum of component tensors, and each of which is treated as an outer product of a matrix (abundances) and a vector (endmember). MV-NTF builds an explicit physical link with LMM. The cost function of MV-NTF is formulated as

$$\min_{\mathbf{A},\mathbf{B},\mathbf{C}} \ \frac{1}{2}\|\mathcal{Y} - \sum_{r=1}^{R} (\mathbf{A}_r \mathbf{B}_r^T) \circ \mathbf{c}_r\|_F^2 + \frac{\delta}{2}\|\mathbf{1}_{I \times J} - \mathbf{A}\mathbf{B}^T\|_F^2 \tag{6}$$

where $\mathcal{Y} \in \mathbb{R}^{I \times J \times K}$ represents the observed HSI data cube with K spectral bands and $I \times J$ pixels; $\mathbf{c}_r$ and $\mathbf{A}_r \mathbf{B}_r^T \in \mathbb{R}^{I \times J}$ are the rth endmember and its associated abundance matrix, respectively; R is the number of endmembers; $\circ$ denotes the outer product of a matrix and a vector; $\mathbf{1}_{I \times J}$ is a matrix with all elements equal to one, and δ is the ASC parameter. The first term is about the reconstruction error and the second term denotes the ASC. The Frobenius norm for a third-order tensor is defined as

$$\|\mathcal{Y}\|_F = \left(\sum_i \sum_j \sum_k y_{ijk}^2 \right)^{\frac{1}{2}}. \tag{7}$$

In the optimization for the cost function (6), each $\mathbf{A}_r \in \mathbb{R}^{I \times L}$ is a component matrix of $\mathbf{A}$, i.e., $\mathbf{A} = [\mathbf{A}_1 \cdots \mathbf{A}_R] \in \mathbb{R}^{I \times RL}$. Similarly, $\mathbf{B}_r \in \mathbb{R}^{J \times L}$, $\mathbf{B} = [\mathbf{B}_1 \cdots \mathbf{B}_R] \in \mathbb{R}^{J \times RL}$, and $\mathbf{C} = [\mathbf{c}_1 \cdots \mathbf{c}_R]$. Here, L denotes the column number of $\mathbf{A}_r$ and $\mathbf{B}_r$, whose value needs to be manually determined and is related to the rank of abundance matrix.

III. Proposed SCNMTF-Based Unmixing Model

A. Motivation

As is well known, high-dimensional tensor-based unmixing methods have a superiority in preserving the intrinsic structure of HSI data than the matrix-based ones. However, for MV-NTF, the forceful rank constraint and the way of directly dealing with data tensor may lead to the loss of local details. In contrast, NMF works in vector space, where unmixing is performed at the pixel level, without requiring compulsory consideration of contextual information. Thus, tiny spatial structures are more easily learned by NMF. There are complementary merits between MV-NTF and NMF.

Fig. 1 displays one set of abundance maps estimated by basic MV-NTF and NMF with only ASC and ANC. This experiment is conducted on synthetic data whose generation process is given in Section IV. From the root-mean-square error (RMSE) results, MV-NTF generally performs better than NMF, demonstrating that the abundance maps by MV-NTF are closer to the real ones. However, the RMSE result obtained by NMF is more desirable when the real abundance map contains more local spatial variations, e.g., Fig. 1(b) and (c). From the visual comparison, it can be evidently observed that the abundance maps estimated by NMF have more exquisite and detailed edges, while MV-NTF yields in smoother abundance maps. This phenomenon is also consistent with the comparison between MV-NTF-based and NTF-based methods in [38], similarly revealing that the tensor works better with smoother images, whereas has no advantage for high-spatial resolution images containing abundant small-scale details.

B. SCNMTF Model

Through the above experimental analysis, it is significant to couple MV-NTF and NMF for incorporating their individual merits. Let MV-NTF and NMF share endmembers and abundances, the cost function of coupled model is formulated as

$$\begin{aligned} \min_{\mathbf{A},\mathbf{B},\mathbf{C},\mathbf{S}} \ & \frac{1}{2}\|\mathcal{Y} - \sum_{r=1}^{R} (\mathbf{A}_r \mathbf{B}_r^T) \circ \mathbf{c}_r\|_F^2 + \frac{1}{2}\|\mathbf{Y} - \mathbf{CS}\|_F^2 \\ & \text{s.t. } \mathcal{F}(\mathbf{s}_r) = \mathbf{A}_r \mathbf{B}_r^T, \ \mathbf{1}_R^T \mathbf{S} = \mathbf{1}_P^T \\ & \mathbf{A} \succeq 0, \ \mathbf{B} \succeq 0, \ \mathbf{C} \succeq 0, \ \mathbf{S} \succeq 0 \end{aligned} \tag{8}$$

where the first and second terms denote the reconstruction errors of tensor factorization and matrix factorization, respectively. Here, $\mathbf{Y}$ is obtained by unfolding the original tensor data $\mathcal{Y}$ into a matrix. $\mathbf{c}_r$ in MV-NTF is the column vector of endmember matrix $\mathbf{C}$ in NMF, for direct endmember sharing. However, due to the totally different representations for abundances in MV-NTF and NMF, abundance sharing cannot be achieved by

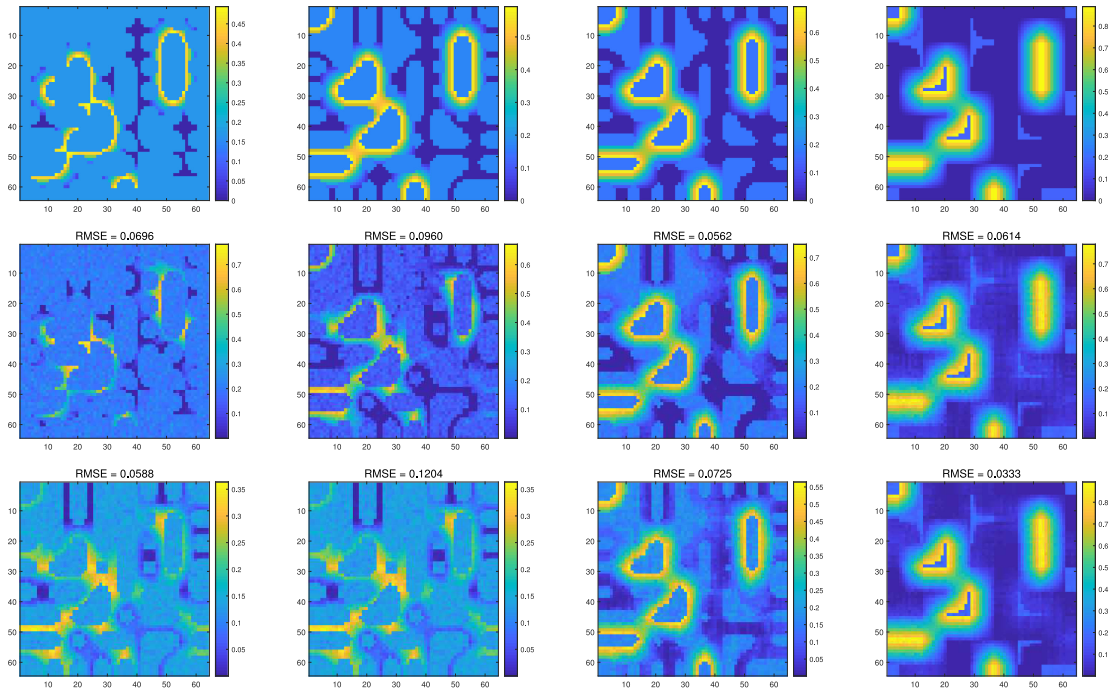

Fig. 1. Abundances of one endmember estimated from synthetic data with different mixing levels (controlled by parameter θ). From top to bottom: reference, NMF, and MV-NTF. (a) $\theta = 0.5$. (b) $\theta = 0.6$. (c) $\theta = 0.7$. (d) $\theta = 0.8$.

directly using the same abundance matrix. As a result, an auxiliary constraint $\mathcal{F}(\mathbf{s}_r) = \mathbf{A}_r\mathbf{B}_r^T$ is presented to impose them equal, wherein the operation $\mathcal{F} : \mathbb{R}^P \longrightarrow \mathbb{R}^{I\times J}$ reshapes $\mathbf{s}_r$ (the rth row vector of $\mathbf{S}$) into an $I \times J$ matrix, and $P = I \times J$. This constraint is an indirect abundance sharing.

As we know, diverse constraints based on intrinsic properties of HSI can further facilitate physical interpretation. Among them, sparsity constraint is a useful scheme to improve unmixing performance, under the assumption that most pixels in HSI are mixed by a small subset of all endmembers. Thus, the widely used $L_{1/2}$ regularizer is embedded into (8) to promote the sparsity of abundances. In the meantime, let the constraint $\mathcal{F}(\mathbf{s}_r) = \mathbf{A}_r\mathbf{B}_r^T$ be absorbed into the equation, then, the cost function of our proposed SCNMTF model is formulated as

$$\begin{aligned}\min_{\mathbf{A},\mathbf{B},\mathbf{C},\mathbf{S}} \ & \frac{1}{2}\|\mathcal{Y} - \sum_{r=1}^{R}(\mathbf{A}_r\mathbf{B}_r^T)\circ\mathbf{c}_r\|_F^2 + \frac{1}{2}\|\mathbf{Y} - \mathbf{CS}\|_F^2 \\ & + \frac{u}{2}\sum_{r=1}^{R}\|\mathcal{F}(\mathbf{s}_r) - \mathbf{A}_r\mathbf{B}_r^T\|_F^2 + \lambda\|\mathbf{S}\|_{1/2} \\ \text{s.t. } & \mathbf{A} \succeq 0,\ \mathbf{B} \succeq 0,\ \mathbf{C} \succeq 0,\ \mathbf{S} \succeq 0,\ \mathbf{1}_R^T\mathbf{S} = \mathbf{1}_P^T \end{aligned} \tag{9}$$

where u controls the similarity between $\mathbf{S}$ and $\sum_r^R \mathbf{A}_r\mathbf{B}_r^T$, and a larger u represents a higher similarity. λ balances the tradeoff between the reconstruction error and the sparseness of $\mathbf{S}$. $\|\mathbf{S}\|_{1/2}$ is defined as

$$\|\mathbf{S}\|_{1/2} = \sum_{r,p=1}^{R,P}(s_{r,p})^{1/2}. \tag{10}$$

C. Optimization

As mentioned in Section II, the optimization of MV-NTF treats all submatrices as a whole, i.e., $\mathbf{A} = [\mathbf{A}_1 \cdots \mathbf{A}_R]$ is updated as an independent variable in iterations. However, the constraint $\|\mathcal{F}(\mathbf{s}_r) - \mathbf{A}_r\mathbf{B}_r^T\|_F^2$ is discrete for the individual submatrice, i.e., $\mathbf{A}_r$ and $\mathbf{B}_r$. For this reason, this constraint term is supposed to be in the same form as the first MV-NTF term to facilitate optimization. To this end, all abundance maps $\mathcal{F}(\mathbf{s}_r)$ for R endmembers are stacked into a tensor $\mathcal{S} \in \mathbb{R}^{I\times J\times R}$, i.e., $\mathcal{S}_{:,:,r} = \mathcal{F}(\mathbf{s}_r)$. Then, the cost function (9) is further reformulated as

$$\begin{aligned}\min_{\mathbf{A},\mathbf{B},\mathbf{C},\mathbf{S}} \ & \frac{1}{2}\|\mathcal{Y} - \sum_{r=1}^{R}(\mathbf{A}_r\mathbf{B}_r^T)\circ\mathbf{c}_r\|_F^2 + \frac{1}{2}\|\mathbf{Y} - \mathbf{CS}\|_F^2 \\ & + \frac{u}{2}\|\mathcal{S} - \sum_{r=1}^{R}(\mathbf{A}_r\mathbf{B}_r^T)\circ\mathbf{e}_r\|_F^2 + \lambda\|\mathbf{S}\|_{1/2} \\ \text{s.t. } & \mathbf{A} \succeq 0,\ \mathbf{B} \succeq 0,\ \mathbf{C} \succeq 0,\ \mathbf{S} \succeq 0,\ \mathbf{1}_R^T\mathbf{S} = \mathbf{1}_P^T \end{aligned} \tag{11}$$

where $\mathbf{e}_r$ is a column vector of length R and is a component of the identity matrix $\mathbf{E} = [\mathbf{e}_1 \cdots \mathbf{e}_R]$.

Now, the optimization problem can be split into the corresponding individual subproblems by ADMM [44], and each one is solved by the augmented multiplicative algorithm. In each iteration, one variable is updated with other variables being fixed to their current values.

1) Update Rules for $\mathbf{A}$ *and* $\mathbf{B}$*:* With other variables being fixed, the suboptimization for $\mathbf{A}$ is presented as

$$\mathcal{G}(\mathbf{A}) = \frac{1}{2}\|\mathbf{Y}_{(1)} - \mathbf{Q}\mathbf{A}^T\|_F^2 + \frac{u}{2}\|\mathbf{S}_{(1)} - \mathbf{M}\mathbf{A}^T\|_F^2 + \mathrm{Tr}(\Phi^T\mathbf{A}) \tag{12}$$

where $\mathbf{Q} = \mathbf{B}\bar{\odot}\mathbf{C}$, $\mathbf{M} = \mathbf{B}\bar{\odot}\mathbf{E}$, and Φ is the Lagrange multiplier. Fixed other variables, the suboptimization for $\mathbf{A}$ is a linear problem. By taking the partial derivative of $\mathcal{G}(\mathbf{A})$ with respect to $\mathbf{A}$

$$\nabla_{\mathbf{A}}\mathcal{G}(\mathbf{A}) = -\mathbf{Y}_{(1)}^T\mathbf{Q} + \mathbf{A}\mathbf{Q}^T\mathbf{Q} - u(\mathbf{S}_{(1)}^T\mathbf{M} - \mathbf{A}\mathbf{M}^T\mathbf{M}) + \Phi. \tag{13}$$

Then, the Karush–Kuhn–Tucker conditions are applied to (13), i.e., $\nabla_{\mathbf{A}}\mathcal{G}(\mathbf{A}) = 0$ and $\Phi .* \mathbf{A} = 0$, resulting in the update rule for $\mathbf{A}$ as

$$\mathbf{A} \leftarrow \mathbf{A} .* (\mathbf{Y}_{(1)}^T\mathbf{Q} + u\mathbf{S}_{(1)}^T\mathbf{M})./(\mathbf{A}\mathbf{Q}^T\mathbf{Q} + u\mathbf{A}\mathbf{M}^T\mathbf{M}). \tag{14}$$

Similarly, the suboptimization for $\mathbf{B}$ is given as

$$\mathcal{G}(\mathbf{B}) = \frac{1}{2}\|\mathbf{Y}_{(2)} - \mathbf{Q}\mathbf{B}^T\|_F^2 + \frac{u}{2}\|\mathbf{S}_{(2)} - \mathbf{M}\mathbf{B}^T\|_F^2 + \mathrm{Tr}(\Psi^T\mathbf{B}) \tag{15}$$

where $\mathbf{Q} = \mathbf{C}\bar{\odot}\mathbf{A}$ and $\mathbf{M} = \mathbf{E}\bar{\odot}\mathbf{A}$. Then, the update rule for $\mathbf{B}$ is

$$\mathbf{B} \leftarrow \mathbf{B} .* (\mathbf{Y}_{(2)}^T\mathbf{Q} + u\mathbf{S}_{(2)}^T\mathbf{M})./(\mathbf{B}\mathbf{Q}^T\mathbf{Q} + u\mathbf{B}\mathbf{M}^T\mathbf{M}). \tag{16}$$

2) Update Rule for $\mathbf{C}$*:* The suboptimization problem for $\mathbf{C}$ is formulated as

$$\mathcal{G}(\mathbf{C}) = \frac{1}{2}\|\mathbf{Y}_{(3)} - \mathbf{Q}\mathbf{C}^T\|_F^2 + \frac{1}{2}\|\mathbf{Y} - \mathbf{C}\mathbf{S}^T\|_F^2 + \mathrm{Tr}(\Gamma^T\mathbf{C}) \tag{17}$$

where $\mathbf{Q} = [(\mathbf{A}_1 \odot \mathbf{B}_1)\mathbf{1}_L \cdots (\mathbf{A}_R \odot \mathbf{B}_R)\mathbf{1}_L]$, and $\mathbf{1}_L$ is the all-one column vector of length L.

Similarly, the update rule for $\mathbf{C}$ is

$$\mathbf{C} \leftarrow \mathbf{C} .* (\mathbf{Y}_{(3)}^T\mathbf{Q} + \mathbf{Y}\mathbf{S}^T)./(\mathbf{C}\mathbf{Q}^T\mathbf{Q} + \mathbf{C}\mathbf{S}\mathbf{S}^T). \tag{18}$$

3) Update Rule for $\mathbf{S}$*:* Since the abundance matrix $\mathbf{S}$ of NMF is discrete in the $\sum_{r=1}^{R}\|\mathcal{F}(\mathbf{s}_r) - \mathbf{A}_r\mathbf{B}_r^T\|_F^2$ term in (12), this term is rewritten as

$$\|\mathbf{S} - \mathbf{H}\|_F^2 \tag{19}$$

where $\mathbf{H}_r = \mathcal{F}^{-1}(\mathbf{A}_r\mathbf{B}_r^T)$ is the ith row in $\mathbf{H}$, and $\mathcal{F}^{-1} : \mathbb{R}^{I\times J} \longrightarrow \mathbb{R}^P$ is the reverse operation of $\mathcal{F}$. Thereby, the suboptimization function for $\mathbf{S}$ is formulated as

$$\mathcal{G}(\mathbf{S}) = \frac{1}{2}\|\mathbf{Y}_f - \mathbf{C}_f\mathbf{S}\|_F^2 + \frac{u}{2}\|\mathbf{S} - \mathbf{H}\|_F^2 + \lambda\|\mathbf{S}\|_{1/2} + \mathrm{Tr}(\Theta^T\mathbf{S}) \tag{20}$$

in which ASC is absorbed into the augmented matrices $\mathbf{Y}_f$ and $\mathbf{C}_f$, and is controlled by β as

$$\mathbf{Y}_f = \begin{bmatrix}\mathbf{Y} \\ \beta\mathbf{1}_P^T\end{bmatrix},\ \mathbf{C}_f = \begin{bmatrix}\mathbf{C} \\ \beta\mathbf{1}_R^T\end{bmatrix}. \tag{21}$$

Algorithm 1: SCNMTF for Hyperspectral Unmixing.

Input: An observed HSI data $\mathcal{Y} \in \mathbb{R}^{I\times J\times K}$.
The number of endmembers R.
The parameters L, u, β, λ.
Output: $\mathbf{C}$ and $\mathbf{S}$.
Initialize: $\mathbf{C}$ and $\mathbf{S}$ by the VCA and FCLS.
$\mathbf{A}$ and $\mathbf{B}$ by the NMF of $\mathbf{S}$.
Repeat:
Update $\mathbf{A}$ by (14).
Update $\mathbf{B}$ by (16).
Update $\mathbf{C}$ by (18).
Update $\mathbf{S}$ by (22).
until the stopping criterion is satisfied.

Then, the update rule for $\mathbf{S}$ is

$$\mathbf{S} \leftarrow \mathbf{S} .* (\mathbf{C}_f^T\mathbf{Y}_f + u\mathbf{H})./(\mathbf{C}_f^T\mathbf{C}_f\mathbf{S} + u\mathbf{S} + \frac{\lambda}{2}\mathbf{S}^{-1/2}). \tag{22}$$

D. Complexity Analysis and Implementation Issues

The optimization procedure for the proposed SCNMTF unmixing algorithm is summarized in Algorithm 1. First, we analyze the computational complexity. For (14) and (16), the number of floating-point operations needed are $RL(4I + 2IJK + 2JKRL + 4IRL + JK + 2IJR + 2JR^2L + JR)$ and $RL(4J + 2IJK + 2IKRL + 4JRL + IK + 2IJR + 2IR^2L + IR)$, respectively; for (18), the number is $R(4K + 4IJK + 4IJR + 4KR + 3IJL)$; and for (22), the number is $R(6IJ + 2IJK + 2KR + 2R + 2IJR + I^2\,J^2R)$. Thus, the computational complexity is $O(tIJKRL + tIKR^2\,L^2 + tJKR^2\,L^2 + tI^2\,J^2R^2)$ after t iterations.

Then, some important preliminaries are discussed in detail. The first issue is the initialization of variable matrices. In our experiments, VCA [7] and FCLS [9] are adopted to initialize the endmember matrix $\mathbf{C}$ and the abundance matrix $\mathbf{S}$, respectively. With regard to $\mathbf{A}$ and $\mathbf{B}$, the rth abundance $\mathcal{F}(\mathbf{s}_r)$ is decomposed into two nonnegative matrices by NMF to initialize $\mathbf{A}_r$ and $\mathbf{B}_r$, respectively.

The second crucial issue is the determination of parameters. There are five parameters R, L, u, β, and λ in our proposed method. The number of endmembers R can be known as a prior knowledge in synthetic data, while determined by an approximation in real data. L controls the rank of abundance matrix, and is set as $L = \frac{2}{3}\min(I, J)$ according to [36]. The determination of u is vital in unmixing, which is related to the strength of coupling. The optimal value for u is determined through the experiments in following section. β controls the ASC and is experientially set to 10. λ is dependent on the sparsity of abundances, hence, its adaptive selection is discussed in next experimental analysis. Besides, it is worth noting that SCNMTF with $\lambda = 0$ becomes CNMTF method.

About the stopping criterion, the main loop in algorithm 1 is terminated by two criteria. One is the maximum iteration number and set to be 2000. The other is a predefined error tolerance for the relative changes of abundance matrix and endmember

matrix, which is set to be 1×10^{-3}. If either one is met, the optimization procedure stops.

IV. Experiments and Discussion

In this section, a series of experiments using synthetic and real hyperspectral data have conducted to verify the effectiveness of our proposed method. TV-RSNMF, $L_{1/2}$-NMF, and MV-NTF are selected for comparison. To evaluate the performance, spectral angle distance (SAD) and RMSE are chosen as quantitative metrics. The SAD is used to measure the dissimilarity of the rth estimated endmember $\hat{\mathbf{c}_r}$ and its real endmember $\mathbf{c}_r$, and is defined by

$$\text{SAD}_r = \arccos\left(\frac{\mathbf{c}_r^T \hat{\mathbf{c}}_r}{\|\mathbf{c}_r^T\| \|\hat{\mathbf{c}}_r\|}\right). \tag{23}$$

The RMSE is used to measure the difference between the rth estimated abundance $\widehat{\mathbf{S}}_r$ and its real abundance $\mathbf{S}_r$, which is defined by

$$\text{RMSE}_r = \left(\frac{1}{P}|\mathbf{S}_r - \widehat{\mathbf{S}}_r|^2\right)^{\frac{1}{2}}. \tag{24}$$

To avoid randomness, each experiment is run ten times and the average result with standard deviation is reported.

A. Experiments on Synthetic Data

Six spectral signatures ($R = 6$) are randomly selected from the U.S. Geological Survey (USGS) digital spectral library for the generation of synthetic data, which are Carnallite NMNH98011, Ammonioalunite NMNH145596, Almandine WS478, Biotite HS28.3B, Axinite HS342.3B, and Chlorite HS179.3B, respectively. The spectrum of each material comprises 224 spectral bands and its reflectance values distribute from 0.38 to 2.5 μm. We adopted the same manner in [36] to create abundance maps and mixed pixels. Details of this generation method are provided as follows: a given image with $z^2 \times z^2$ pixels is divided into z^2 regions, each of which is filled with a kind of endmember randomly. Then, a spatial low-pass filter $((z+1) \times (z+1))$ is applied to generate mixed pixels. In order to eliminate pure pixels, if the abundance of a pixel is larger than the threshold θ ($0 \leq \theta \leq 1$), the pixel will be replaced by a mixture of all six endmembers with equal proportions. After clean synthetic data is produced, Gaussian noise is further added. The noise level is determined by signal-to-noise (SNR), and is defined as

$$\text{SNR} = 10\log_{10}\frac{E[\mathbf{y}^t\mathbf{y}]}{E[\mathbf{n}^t\mathbf{n}]} \tag{25}$$

where $E[\cdot]$ denotes the expectation operator, $\mathbf{y}$ is the clean synthetic pixel, and $\mathbf{n}$ is the additive noise.

1) Parameter Analysis: The most crucial parameter μ controls the similarity of abundances between two decompositions. In other words, μ is in charge of the coupling level between NMF and MV-NTF. In this experiment, six different values of the parameter μ (1, 5, 10, 50, $1e2$, $1e3$) are tested with other parameters fixed, i.e., sparse regularization parameter $\lambda = 0$, image size 64×64 ($z = 8$), mixing level $\theta = 0.8$, and SNR $= 20$ dB. Fig. 2 depicts the SAD and RMSE results with standard deviation. Obviously, the unmixing performance is stable when μ is in the range [1,100]. Then, the value of μ is fixed to 10 in the following experiments.

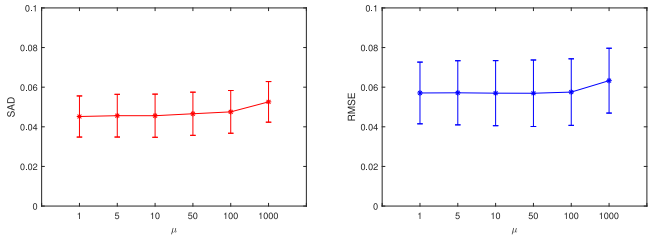

Fig. 2. Performance of SCNMTF with respect to parameter μ.

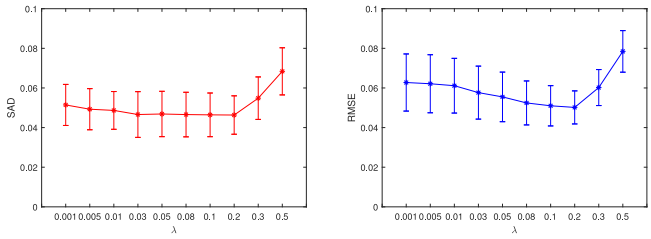

Fig. 3. Performance of SCNMTF with respect to parameter λ.

Next, we analyze the effect of parameter λ. Other parameters of data generation are set to the same as before. The test values for λ are $\{1e\text{-}3, 5e\text{-}3, 1e\text{-}2, 3e\text{-}2, 5e\text{-}2, 8e\text{-}2, 0.1, 0.2, 0.3, 0.5\}$. The SAD and RMSE results are shown in Fig. 3. It can be seen that the values of SAD and RMSE are stable when λ is less than 0.2. It is worth noting that when the value of λ is close to 0 (the sparsity constraint is weak in these cases), the SAD and RMSE values increase, which means sparsity constraint has a positive effect on unmixing. On account of the sparsity related to the actual abundances, λ is set to 0.05 in all synthetic data experiments for simplicity.

2) Different Noise Levels: The synthetic data are generated by $\theta = 0.8$, $z = 8$. SNR varies from 15, 20, 25, 30 to 40 dB. As shown in Fig. 4, the performances of all algorithms decrease with the increase of noise. Note that both of CNMTF and MV-NTF yield relatively poor results when SNR is small, which demonstrates the advantage of sparsity constraint in high noise level scenarios. Meanwhile, CNMTF yields more accurate results than MV-NTF, indicating the availability of coupling. Also, the SAD and RMSE of SCNMTF are slightly lower than that of CNMTF when SNR is small, which is probably because the strength of sparsity constraint is too strong. Overall, SCNMTF and CNMTF perform better than other three alternatives under different SNRs.

3) Different Mixing Levels: The mixing level is controlled by parameter θ. A smaller θ value means a higher mixing level, resulting in more difficulties for unmixing. The synthetic data are produced by $z = 8$ and SNR$=$ 20 dB, and the value of θ changes from 0.5, 0.6, 0.7, 0.8, 0.9 to 1. The results are presented in Fig. 5. As can be seen, all algorithms perform better along with θ increases. Note that SCNMTF is superior to other alternatives,

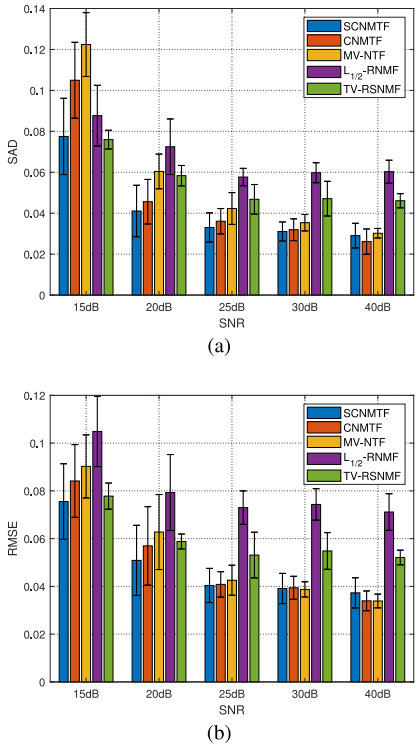

Fig. 4. Results of (a) SAD and (b) RMSE with different noise levels.

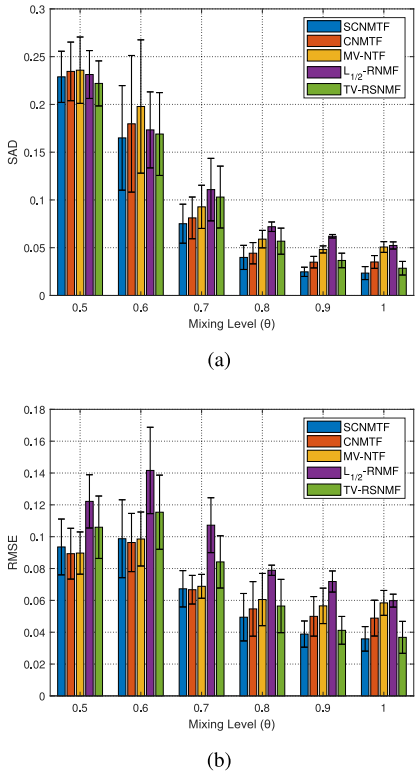

Fig. 5. Results of (a) SAD and (b) RMSE with different mixing levels.

revealing its effectiveness in exploiting structure information. Furthermore, it is found that the RMSE of SCNMTF is slightly worse than that of CNMTF when θ is 0.5 and 0.6. This is probably because a high mixing level results in a poor sparsity, which restricts the availability of sparsity constraint.

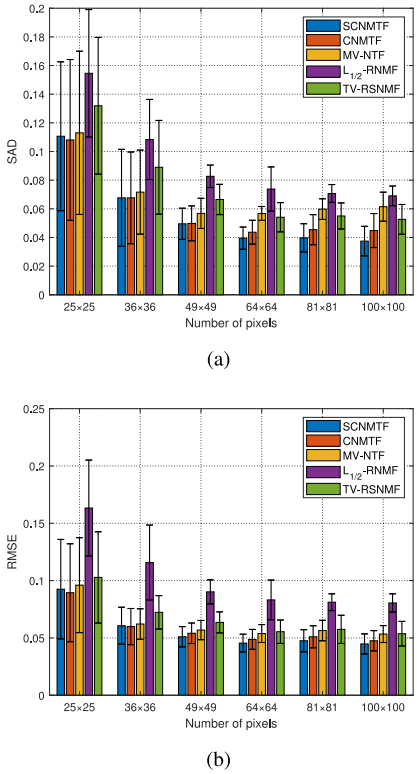

Fig. 6. Results of (a) SAD and (b) RMSE with different number of pixels.

4) Different Number of Pixels: More pixels contain more intrinsic information, which is more favourable for unmixing. The image size is selected as 25×25, 36×36, 49×49, 64×64, 81×81, and 100×100, corresponding to $z = 5, 6, \ldots, 10$. Fig. 6 plots the results at $\theta = 0.8$ and SNR $= 20$ dB. As expected, the values of SAD and RMSE for five algorithms gradually decrease and tend to be stable as the size of synthetic data grows. Moreover, the results obtained by CNMTF and SCNMTF are more accurate than those of three other algorithms. CNMTF performs a little better than SCNMTF when the number of pixels is 25×25. This is mainly because the fixed value of λ (0.05) is too large when the number of pixels is small, so that the sparsity constraint is counterproductive. In addition, the discrepancy between MV-NTF and our proposed coupled method is more obvious as the number of pixels increases. Therefore, the superiority of our proposed method in exploiting data intrinsic information is further validated.

5) Incorrect Number of Endmembers: The aim of this experiment is to measure the unmixing accuracy when the estimated number of endmembers is inaccurate, because this situation is common in practical applications. To do this, the value of R varies from 4 to 8, and the actual number of endmembers in synthetic data is 6. Other parameters are the same as before. As shown in Fig. 7, all algorithms achieve the best performance when the number of endmembers is estimated correctly (i.e., $R = 6$). Note that both of SADs and RMSEs for the five algorithms show a sharp increase with the estimated R is too less than

TABLE I
MEANS AND STANDARD DEVIATIONS OF SAD BY DIFFERENT METHODS WITH THE CUPRITE DATA SET

Methods	SCNMTF	CNMTF	MV-NTF	$L_{1/2}$-NMF	TV-RSNMF
Alunite GDS82 Na82	0.1087±1.05%	**0.1027±1.53%**	0.1114±1.72%	0.1340±6.29%	0.1157±1.72%
Andradite WS487	0.0834±2.15%	0.0869±2.34%	0.0853±1.95%	**0.0731±1.66%**	0.0831±2.04%
Buddingtonite GDS85 D-206	0.0903±1.51%	**0.0878±1.98%**	0.0882±2.22%	0.1032±3.20%	0.0973±0.92%
Chalcedony CU91-6A	0.1446±1.22%	0.1532±1.78%	0.1521±2.65%	0.1504±1.53%	**0.1406±1.60%**
Kaolin/Smect H89-FR-5 30K	0.0624±1.73%	0.0694±1.80%	0.0771±2.04%	0.1004±3.83%	**0.0524±1.05%**
Kaolin/Smect KLF508 85%K	0.0962±2.85%	0.0964±2.92%	**0.0879±2.04%**	0.1163±3.78%	0.1215±4.46%
Kaolinite KGa-2	0.1386±3.36%	0.1435±3.82%	0.1634±4.97%	0.1520±5.67%	**0.1352±2.81%**
Montmorillonite+Illi CM37	0.0591±2.16%	0.0636±2.42%	0.0699±2.83%	0.0583±1.19%	**0.0483±0.49%**
Muscovite IL107	0.0962±1.55%	0.0933±1.19%	**0.0930±1.00%**	0.1045±2.59%	0.1021±0.86%
Nontronite NG-1.a	0.1135±1.83%	0.1181±2.07%	0.1227±3.09%	0.1261±1.34%	**0.1086±1.48%**
Pyrope WS474	**0.0803±1.07%**	0.0825±1.60%	0.0839±1.94%	0.1134±2.55%	0.0970±2.27%
Sphene HS189.3B	0.0761±0.75%	**0.0651±0.60%**	0.0695±0.81%	0.0680±1.69%	0.1028±1.62%
Mean	**0.0958±0.40%**	0.0969±0.34%	0.1003±0.26%	0.1083±0.72%	0.1004±0.28%

The minimum value is marked in bold, and the second minimum is underlined.

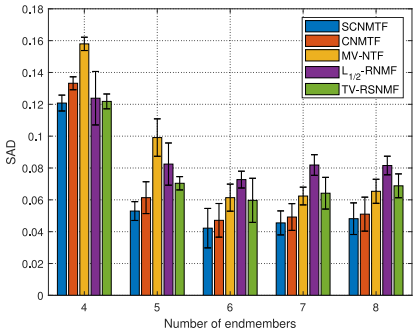

(a)

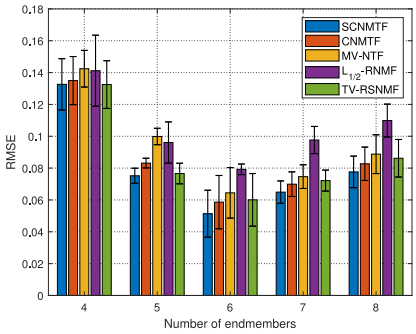

(b)

Fig. 7. Results of (a) SAD and (b) RMSE versus incorrect number of endmembers.

the actual endmember number (i.e., $R = 4$). Most importantly, SCNMTF still outperforms others in all cases.

6) Comparison of Running Time: Last, the average running time of ten trials for each method was recorded, at SNR = 20 dB and $\theta = 0.8$. All the experiments are implemented in MATLAB R2018a on a personal computer with Inter Core i5 CPU @ 1.60 GHz and 8.00 GB RAM. The running time of SCNMTF, CNMTF, MV-NTF, $L_{1/2}$-NMF, and TV-RSNMF is 364.2 s, 360.2 s, 421.4 s, 18.4 s, and 30.6 s, respectively. It can be found that the proposed method reduces the running time than the original MV-NTF, which is probably because that the solution space is shrunk by coupling.

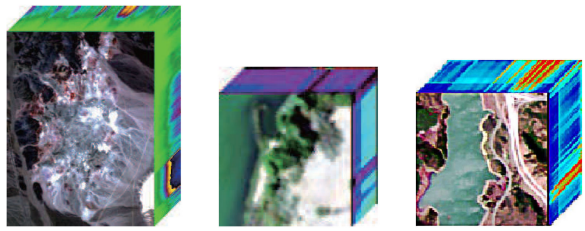

(a) (b) (c)

Fig. 8. (a) Cuprite subimage. (b) Samson subimage. (c) Jasper Ridge subimage.

B. Experiments on Real Data

1) Cuprite Data set: In order to evaluate the effectiveness of our proposed method in real scenarios, we apply it to three real hyperspectral data sets. The first data set is a subset extracted from the well-known Cuprite data set captured by AVIRIS, which consists of 250×191 pixels and is illustrated in Fig. 8(a). The original data are composed of 224 spectral channels with the wavelength range of 0.4 to 2.5 μm. A total of 188 bands are remained in our experiment after removing water absorption and low SNR bands. The actual number of endmembers presented in Cuprite data has not yet been definitive. Thus, the number of endmembers R is set to 12 according to [45]. Since the reference abundance maps of Cuprite data are unavailable, only the SAD values of all methods are measured to compare.

In this experiment, the parameters u and λ are set to 10 and 0.2, respectively. The SAD results of all methods are listed in Table I. Apparently, the lowest mean SAD is obtained by SCNMTF. Besides, CNMTF also achieves a satisfactory performance. The comparisons of four signatures extracted by different methods with the reference spectra are displayed in Fig. 9. The abundance maps for each endmember estimated by SCNMTF are shown in Fig. 10.

2) Samson Data set: The Samson data set contains 952×952 pixels and 156 bands with the wavelengths from 0.401 to 0.889 μm. Due to the original image is too large, a subset

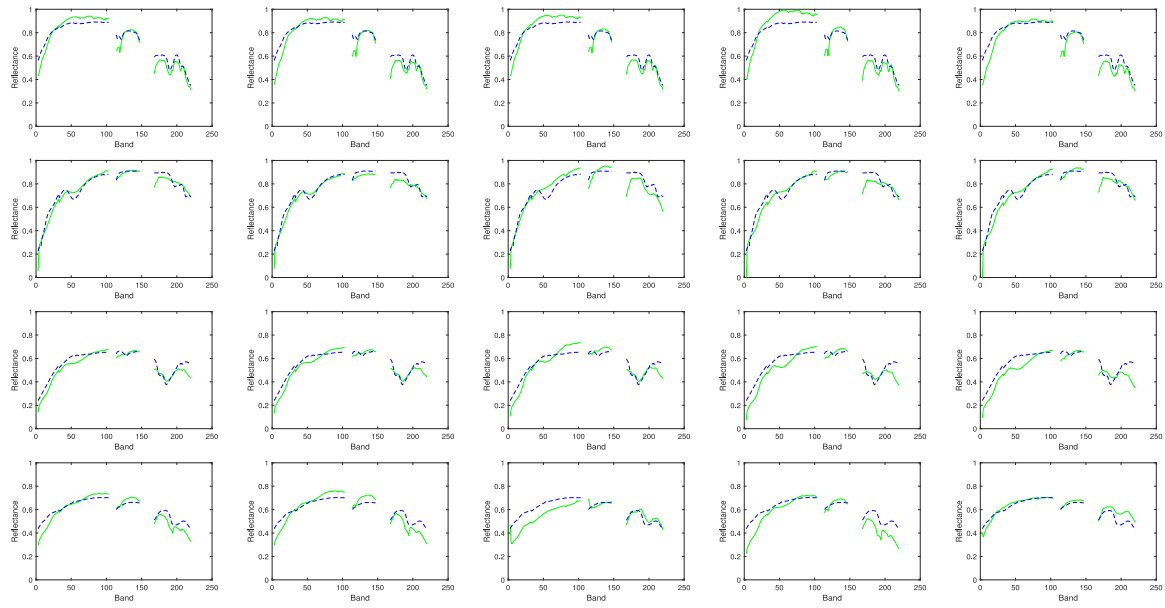

Fig. 9. Cuprite results: Comparisons of the (blue dotted line) USGS library spectra with the (green solid line) signatures extracted by different methods of four endmembers. From top to bottom: Alunite GDS82 Na82, Andradite WS487, Buddingtonite GDS85 D-206, and Chalcedony CU91-6 A. From left to right: (a) SCNMTF. (b) CNMTF. (c) MV-NTF. (d) $L_{1/2}$-NMF. (e) TV-RSNMF.

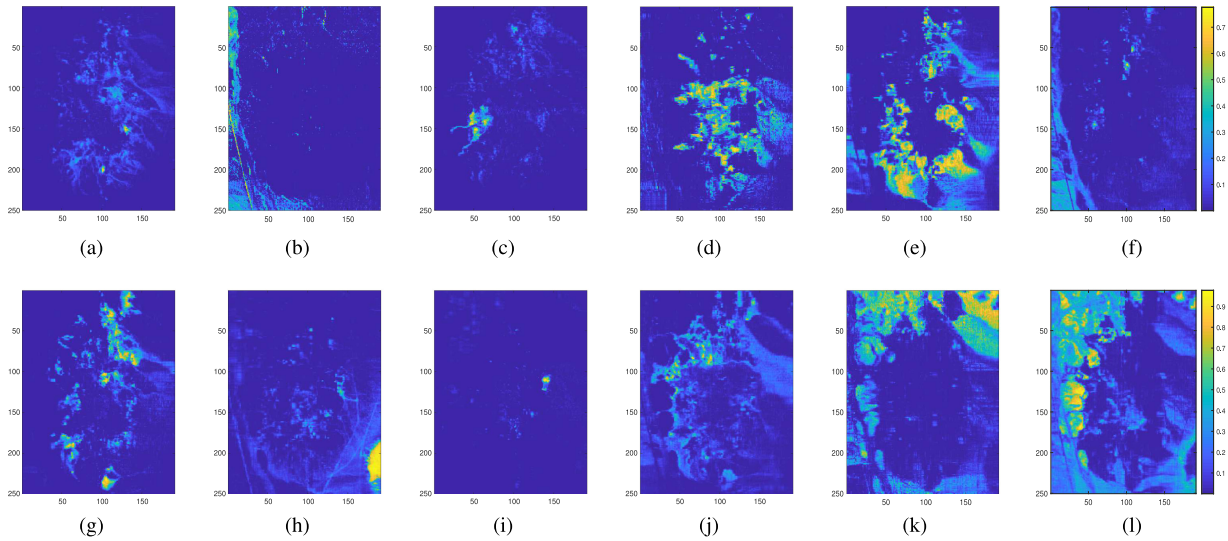

Fig. 10. Cuprite results: Abundance maps estimated by SCNMTF of the 12 endmembers. (a) Alunite GDS82 Na82. (b) Andradite WS487. (c) Buddingtonite GDS85 D-206. (d) Chalcedony CU91-6 A. (e) Kaolin/Smect H89-FR-5 30 K. (f) Kaolin/Smect KLF508 85%K. (g) Kaolinite KGa-2. (h) Montmorillonite+Illi CM37. (i) Muscovite IL107. (j) Nontronite NG-1.a. (k) Pyrope WS474. (l) Sphene HS189.3B.

TABLE II
MEANS AND STANDARD DEVIATIONS OF SAD BY DIFFERENT METHODS WITH THE SAMSON DATA SET

Methods	SCNMTF	CNMTF	MV-NTF	$L_{1/2}$-NMF	TV-RSNMF
Soil	**0.0247±0.07%**	0.0268±0.07%	0.0290±0.07%	0.0272±0.02%	0.0315±0.14%
Tree	0.0496±0.12%	0.0519±0.14%	0.0544±0.16%	**0.0368±0.03%**	0.0526±0.13%
Water	**0.1016±0.15%**	0.1057±0.43%	0.1157±0.69%	0.1568±0.16%	0.1148±0.48%
Mean	**0.0586±0.11%**	0.0615±0.21%	0.0664±0.30%	0.0736±0.07%	0.0660±0.07%

The minimum value is marked in bold and the second minimum is underlined.

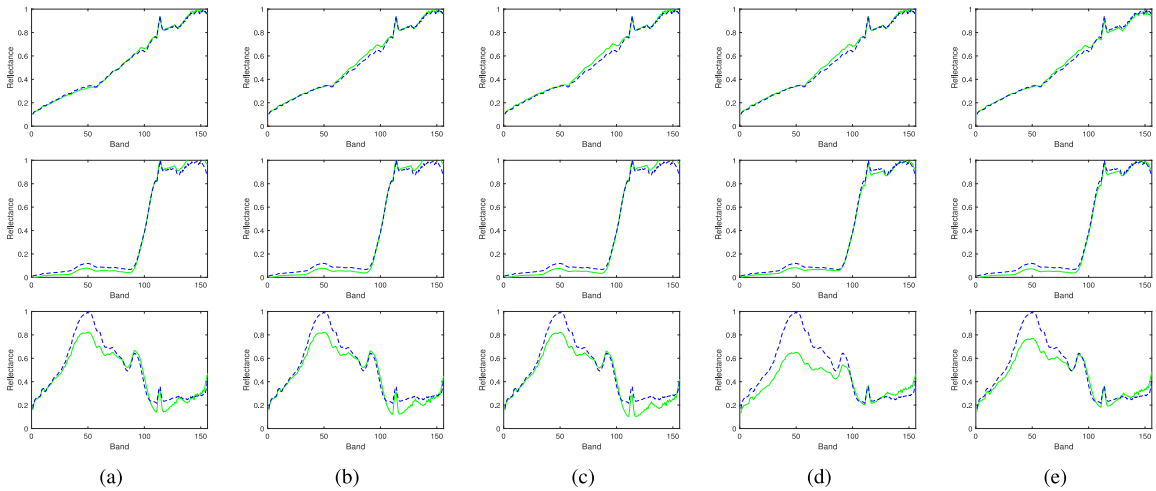

Fig. 11. Samson results: Comparisons of the (blue dotted line) USGS library spectra with the (green solid line) signatures extracted by different methods. From top to bottom: Soil, Tree, and Water. From left to right: (a) SCNMTF. (b) CNMTF. (c) MV-NTF. (d) $L_{1/2}$-NMF. (e) TV-RSNMF.

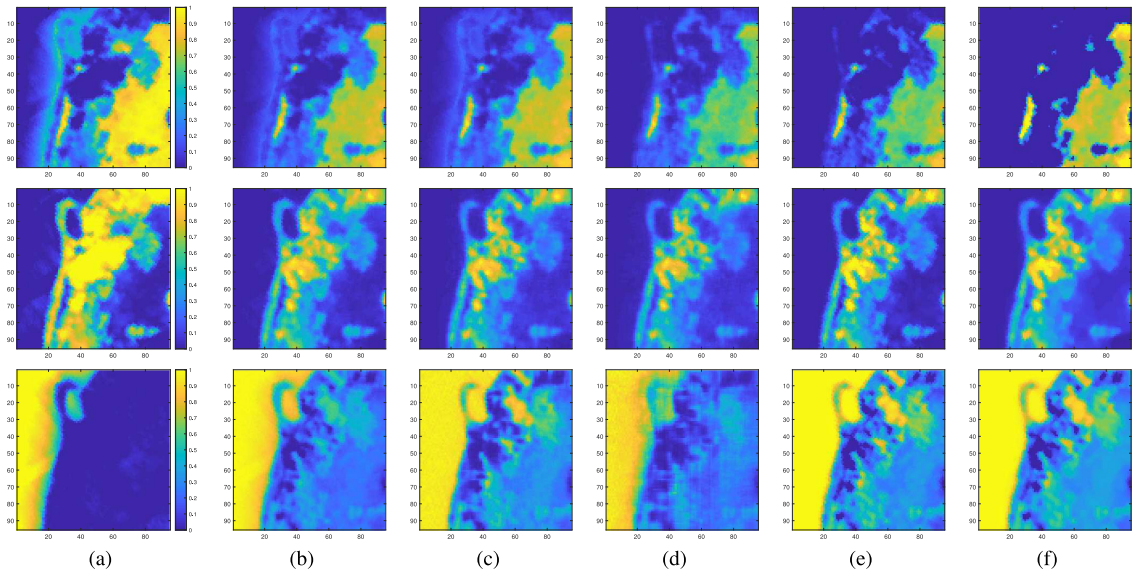

Fig. 12. Samson results: Abundance maps estimated by different methods. From top to bottom: soil, tree, and water. From left to right: (a) Reference. (b) SCNMTF. (c) CNMTF. (d) MV-NTF. (e) $L_{1/2}$-NMF. (f) TV-RSNMF.

composed of 95×95 pixels is utilized in this experiment and is shown in Fig. 8(b). It assumes that three endmembers are present in the Samson data set, which are soil, tree, and water, respectively. In this experiment, λ is set to 0.5. The SAD results of all methods are listed in Table II. Among them, SCNMTF still obtains the smallest mean value of SAD. Since the reference spectra and abundance maps of Samson data set are available, the comparisons of signatures and abundance maps by different methods are displayed in Figs. 11 and 12, respectively. Obviously, the most of signatures and abundance maps extracted by SCNMTF best match the reference ones. The abundance maps of SCNMTF and CNMTF characterize more features than that of MV-NTF.

3) Jasper Ridge Data set: The Jasper Ridge data set is composed of 512×614 pixels and contains 224 bands with the wavelength range of 0.38–2.5 μm. A subimage with 100×100 pixels and 198 bands is selected in this experiment, and is shown in Fig. 8(c). Four endmembers are assumed to exist in the Jasper data set, which are soil, water, tree, and road, respectively. In this experiment, λ is set to 1. Table III lists the SAD values by five methods. From the Table, it can be observed that the mean value of SAD by SCNMTF is the smallest. The visual comparisons for the estimated signatures and abundance maps by all methods are presented in Figs. 13 and 14, respectively. This experiment also reveals that the proposed method outperforms other state-of-the-art algorithms.

TABLE III
MEANS AND STANDARD DEVIATIONS OF SAD BY DIFFERENT METHODS WITH THE JASPER RIDGE DATA SET

Methods	SCNMTF	CNMTF	MV-NTF	$L_{1/2}$-NMF	TV-RSNMF
Tree	**0.1439±2.73%**	0.1629±2.64%	0.1603±4.04%	0.1585±4.07%	0.1644±7.03%
Water	0.1534±8.32%	0.1741±5.66%	0.1819±5.07%	**0.1287±5.04%**	0.2101±7.04%
Soil	**0.0793±2.36%**	0.0943±4.20%	0.1207±5.54%	0.2044±3.11%	0.1380±10.52%
Road	0.6145±5.84%	0.6014±11.46%	0.6197±22.64%	0.6350±8.65%	**0.5138±17.69%**
Mean	**0.2478±2.75%**	0.2582±2.32%	0.2707±4.86%	0.2816±1.86%	0.2565±3.79%

The minimum value is marked in bold and the second minimum is underlined.

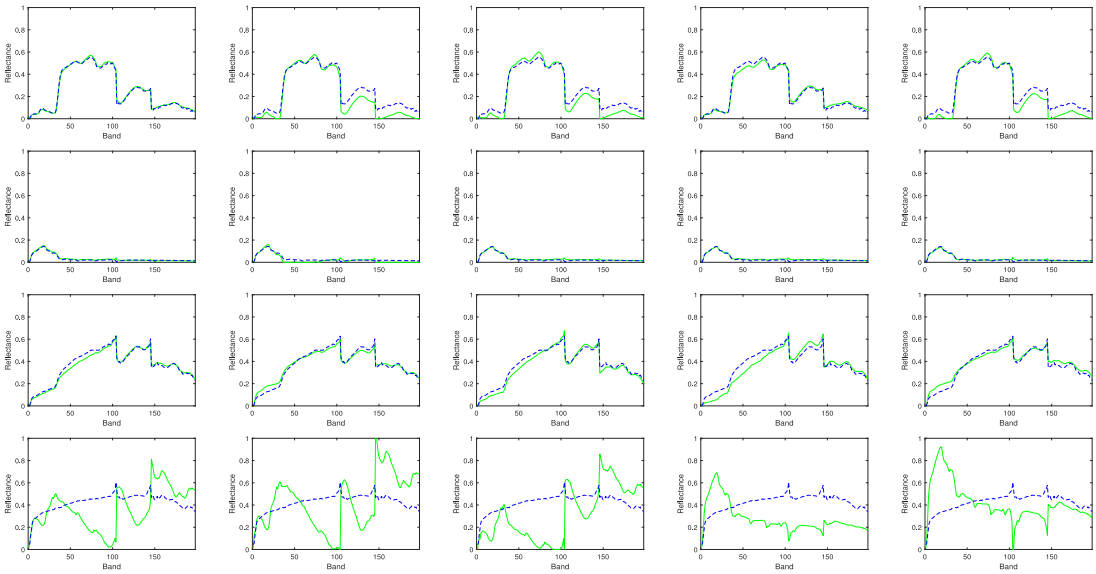

Fig. 13. Jasper Ridge results: Comparisons of the (blue dotted line) USGS library spectra with the (green solid line) signatures extracted by different methods. From top to bottom: tree, water, soil, and road. From left to right: (a) SCNMTF. (b) CNMTF. (c) MV-NTF. (d) $L_{1/2}$-NMF. (e) TV-RSNMF.

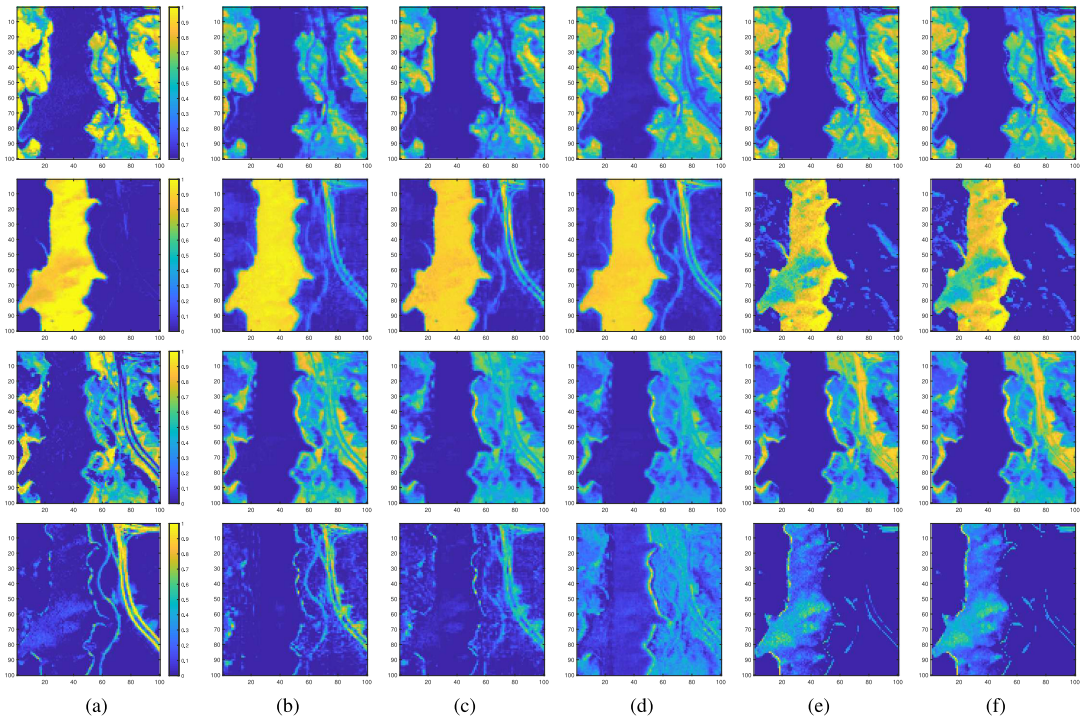

Fig. 14. Jasper Ridge results: Abundance maps estimated by different methods. From top to bottom: tree, water, soil, and road. From left to right: (a) Reference. (b) SCNMTF. (c) CNMTF. (d) MV-NTF. (e) $L_{1/2}$-NMF. (f) TV-RSNMF.

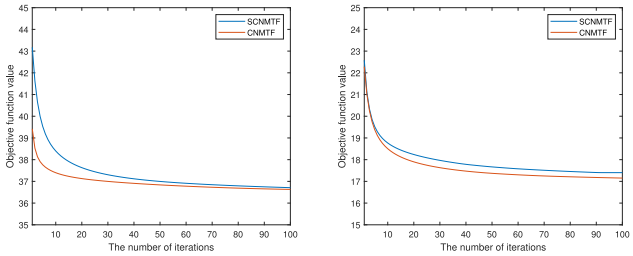

Fig. 15. Convergence analysis of the proposed SCNMTF and CNMTF. (a) Synthetic data. (b) Samson data.

C. Convergence Analysis

In order to investigate the convergence of the proposed SCNMTF and CNMTF, we experimentally records the objective function values in each iteration over synthetic and real hyperspectral data. The synthetic data are generated by $\theta = 0.8$, $z = 8$, and SNR $= 20$ dB. The convergence curves are illustrated in Fig. 15, where the maximum number of iterations $T_{\max}$ is set to 1000. From Fig. 15, all the objective function values decrease monotonically and converge along with the number of iterations increases, which verifies the convergence of SCNMTF and CNMTF.

V. Conclusion

In this article, we present a novel coupled nonnegative matrix–tensor factorization framework for hyperspectral unmixing, which aims at taking the advantages of decompositions over different dimensional spaces by the multi-view coupling. A given HSI data is represented by a tensor and an unfolded matrix simultaneously, then jointly decomposed by coupled MV-NTF and NMF through sharing endmembers and abundances. However, the abundance sharing cannot be achieved by directly using the same abundance variable owing to the distinct representations for abundances in MV-NTF and NMF. Thus, an auxiliary constraint is introduced to enforce these two abundances equal. In addition, the $L_{1/2}$ regularizer is imposed to promote the sparsity of abundances. The proposed SCNMTF method can retain the advantage of MV-NTF in preserving the structure information of HSI, and utilize NMF to exploit more detailed spatial structures. A series of experiments on synthetic and real hyperspectral data have manifested that our proposed method outperforms other benchmarking algorithms. Nevertheless, we mainly focus on exploring spatial information in SCNMTF. In our future work, some prior information about endmembers can be introduced into this model to further enhance unmixing performance.

References

[1] L. Pan, H.-C. Li, H. Meng, W. Li, Q. Du, and W. J. Emery, "Hyperspectral image classification via low-rank and sparse representation with spectral consistency constraint" *IEEE Geosci. Remote Sens. Lett.*, vol. 14, no. 11, pp. 2117–2121, Nov. 2017.

[2] X. Bai, H. Zhang, and J. Zhou, "VHR object detection based on structural feature extraction and query expansion" *IEEE Trans. Geosci. Remote Sens.*, vol. 52, no. 10, pp. 6508–6520, Oct. 2014.

[3] N. Yokoya, T. Yairi, and A. Iwasaki, "Coupled nonnegative matrix factorization unmixing for hyperspectral and multispectral data fusion" *IEEE Trans. Geosci. Remote Sens.*, vol. 50, no. 2, pp. 528–537, Feb. 2012.

[4] J. M. Bioucas-Dias, A. Plaza, N. Dobigeon, M. Parente, Q. Du, P. Gader, and J. Chanussot, "Hyperspectral unmixing overview: Geometrical, statistical, and sparse regression-based approaches" *IEEE J. Sel. Topics Appl. Earth Observ. Remote Sens.*, vol. 5, no. 2, pp. 354–379, Apr. 2012.

[5] J. Wang and C.-I. Chang, "Applications of independent component analysis in endmember extraction and abundance quantification for hyperspectral imagery" *IEEE Trans. Geosci. Remote Sens.*, vol. 44, no. 9, pp. 2601–2616, Sep. 2006.

[6] M. E. Winter, "N-FINDR: An algorithm for fast autonomous spectral end-member determination in hyperspectral data" *Proc. SPIE*, vol. 3753, pp. 266–275, Oct. 1999.

[7] J. M. P. Nascimento and J. M. B. Dias, "Vertex component analysis: A fast algorithm to unmix hyperspectral data" *IEEE Trans. Geosci. Remote Sens.*, vol. 43, no. 4, pp. 898–910, Apr. 2005.

[8] J. Li and J. M. Bioucas-Dias, "Minimum volume simplex analysis: A fast algorithm to unmix hyperspectral data" in *Proc. IEEE Int. Geosci. Remote Sens. Symp*, 2008, pp. 4418–4432.

[9] D. C. Heinz and Chein-I-Chang, "Fully constrained least squares linear spectral mixture analysis method for material quantification in hyperspectral imagery" *IEEE Trans. Geosci. Remote Sens.*, vol. 39, no. 3, pp. 529–545, Mar. 2001.

[10] J. M. Bioucas-Dias and M. A. T. Figueiredo, "Alternating direction algorithms for constrained sparse regression: Application to hyperspectral unmixing" in *Proc. 2nd Workshop Hyperspectral Image Signal Process.: Evol. Remote Sens.*, Jun. 2010, pp. 1–4.

[11] M.-D. Iordache, J. M. Bioucas-Dias, and A. Plaza, "Collaborative sparse regression for hyperspectral unmixing" *IEEE Trans. Geosci. Remote Sens.*, vol. 52, no. 1, pp. 341–354, Jan. 2014.

[12] R. Wang, H.-C. Li, A. Pizurica, J. Li, A. Plaza, and W. J. Emery, "Hyperspectral unmixing using double reweighted sparse regression and total variation" *IEEE Geosci. Remote Sens. Lett.*, vol. 14, no. 7, pp. 1146–1150, Jul. 2017.

[13] M. Berman, H. Kiiveri, R. Lagerstrom, A. Ernst, R. Dunne, and J. F. Huntington, "ICE: A statistical approach to identifying endmembers in hyperspectral images" *IEEE Trans. Geosci. Remote Sens.*, vol. 42, no. 10, pp. 2085–2095, Oct. 2004.

[14] D. C. Zanotta, V. Haertel, Y. E. Shimabukuro, and C. D. Renno, "Linear spectral mixing model for identifying potential missing endmembers in spectral mixture analysis" *IEEE Trans. Geosci. Remote Sens.*, vol. 52, no. 5, pp. 3005–3012, May 2014.

[15] S. Jia and Y. Qian, "Constrained nonnegative matrix factorization for hyperspectral unmixing" *IEEE Trans. Geosci. Remote Sens.*, vol. 47, no. 1, pp. 161–173, Jan. 2009.

[16] L. Miao and H. Qi, "Endmember extraction from highly mixed data using minimum volume constrained nonnegative matrix factorization" *IEEE Trans. Geosci. Remote Sens.*, vol. 45, no. 3, pp. 765–777, Mar. 2007.

[17] Y. Qian, S. Jia, J. Zhou, and A. Robles-Kelly, "Hyperspectral unmixing via $L_{1/2}$ sparsity-constrained nonnegative matrix factorization" *IEEE Trans. Geosci. Remote Sens.*, vol. 49, no. 11, pp. 4282–4297, Nov. 2011.

[18] D. D. Lee and H. S. Seung, "Learning the parts of objects by non-negative matrix factorization" *Nature*, vol. 401, no. 6755, pp. 788–791, Oct. 1999.

[19] V. P. Pauca, J. Piper, and R. J. Plemmons, "Nonnegative matrix factorization for spectral data analysis" *Linear Algebra Appl.*, vol. 416, no. 1, pp. 29–47, Jul. 2006.

[20] N. Wang, B. Du, and L. Zhang, "An endmember dissimilarity constrained non-negative matrix factorization method for hyperspectral unmixing" *IEEE J. Sel. Topics Appl. Earth Observ. Remote Sens.*, vol. 6, no. 2, pp. 554–569, Apr. 2013.

[21] W. He, H. Zhang, and L. Zhang, "Sparsity-regularized robust non-negative matrix factorization for hyperspectral unmixing" *IEEE J. Sel. Topics Appl. Earth Observ. Remote Sens.*, vol. 9, no. 9, pp. 4267–4279, Sep. 2016.

[22] J. Sigurdsson, M. O. Ulfarsson, and J. R. Sveinsson, "Hyperspectral unmixing with l_q regularization," *IEEE Trans. Geosci. Remote Sens.*, vol. 52, no. 11, pp. 6793–6806, Nov. 2014.

[23] F. Zhu, Y. Wang, B. Fan, S. Xiang, G. Meng, and C. Pan, "Spectral unmixing via data-guided sparsity" *IEEE Trans. Image Process.*, vol. 23, no. 12, pp. 5412–5427, Dec. 2014.

[24] Z. Xu, H. Zhang, Y. Wang, X. Chang, and Y. Liang, "$L_{1/2}$ regularization" *Sci. China Inf. Sci.*, vol. 53, no. 6, pp. 1159–1169, May 2010.

[25] M.-D. Iordache, J. M. Bioucas-Dias, and A. Plaza, "Total variation spatial regularization for sparse hyperspectral unmixing" *IEEE Trans. Geosci. Remote Sens.*, vol. 50, no. 11, pp. 4484–4502, Nov. 2012.
[26] W. He, H. Zhang, and L. Zhang, "Total variation regularized reweighted sparse nonnegative matrix factorization for hyperspectral unmixing" *IEEE Trans. Geosci. Remote Sens.*, vol. 55, no. 7, pp. 3909–3921, Jul. 2017.
[27] X. Lu, H. Wu, Y. Yuan, P. Yan, and X. Li, "Manifold regularized sparse NMF for hyperspectral unmixing" *IEEE Trans. Geosci. Remote Sens.*, vol. 51, no. 5, pp. 2815–2826, May 2013.
[28] M. Wang, B. Zhang, X. Pan, and S. Yang, "Group low-rank nonnegative matrix factorization with semantic regularizer for hyperspectral unmixing" *IEEE J. Sel. Topics Appl. Earth Observ. Remote Sens.*, vol. 11, no. 4, pp. 1022–1029, Apr. 2018.
[29] B. Du, M. Zhang, L. Zhang, R. Hu, and D. Tao, "PLTD: Patch-based low-rank tensor decomposition for hyperspectral images" *IEEE Trans. Multimedia*, vol. 19, no. 1, pp. 67–79, Jan. 2017.
[30] Z. Zhong, B. Fan, J. Duan, L. Wang, K. Ding, S. Xiang, and C. Pan, "Discriminant tensor spectral-spatial feature extraction for hyperspectral image classification" *IEEE Geosci. Remote Sens. Lett*, vol. 12, no. 5, pp. 1028–1032, May 2015.
[31] X. Guo, X. Huang, L. Zhang, and L. Zhang, "Hyperspectral image noise reduction based on rank-1 tensor decomposition" *ISPRS J. Photogram. Remote Sens.*, vol. 83, pp. 50–63, Sep. 2013.
[32] Q. Zhang, H. Wang, R. J. Plemmons, and V. P. Pauca, "Spectral unmixing using nonnegative tensor factorization" in *Proc. 45th Annu. Southeast Regional Conf.*, 2007, pp. 531–532.
[33] Q. Zhang, H. Wang, R. J. Plemmons, and V. P. Pauca, "Tensor methods for hyperspectral data analysis: A space object material identification study" *J. Soc. Amer. A*, vol. 25, no. 12, pp. 3001–3012, 2008.
[34] A. Huck and M. Guillaume, "Estimation of the hyperspectral tucker ranks" in *Proc. IEEE Int. Conf. Acoust., Speech Signal Process* Apr. 2009, pp. 1281–1284.
[35] M. A. Veganzones, J. E. Cohen, R. C. Farias, J. Chanussot, and P. Comon, "Nonnegative tensor CP decomposition of hyperspectral data" *IEEE Trans. Geosci. Remote Sens.*, vol. 54, no. 5, pp. 2577–2588, May 2016.
[36] Y. Qian, F. Xiong, S. Zeng, J. Zhou, and Y. Y. Tang, "Matrix-vector nonnegative tensor factorization for blind unmixing of hyperspectral imagery" *IEEE Trans. Geosci. Remote Sens.*, vol. 55, no. 3, pp. 1776–1792, Mar. 2017.
[37] L. D. Lathauwer and D. Nion, "Decompositions of a higher-order tensor in block termspart III: Alternating least squares algorithms" *SIAM J. Matrix Anal. Appl.*, vol. 30, no. 3, pp. 1067–1083, Jan. 2008.
[38] B. Feng and J. Wang, "Constrained nonnegative tensor factorization for spectral unmixing of hyperspectral images: A case study of urban impervious surface extraction" *IEEE Geosci. Remote Sens. Lett.*, vol. 16, no. 4, pp. 583–587, Apr. 2019.
[39] F. Xiong, Y. Qian, J. Zhou, and Y. Y. Tang, "Hyperspectral unmixing via total variation regularized nonnegative tensor factorization" *IEEE Trans. Geosci. Remote Sens.*, vol. 57, no. 4, pp. 2341–2357, Apr. 2019.
[40] N. Yokoya, T. Yairi, and A. Iwasaki, "Coupled nonnegative matrix factorization unmixing for hyperspectral and multispectral data fusion" *IEEE Trans. Geosci. Remote Sens.*, vol. 50, no. 2, pp. 528–537, Feb. 2012.
[41] S. Li, R. Dian, L. Fang, and J. M. Bioucas-Dias, "Fusing hyperspectral and multispectral images via coupled sparse tensor factorization" *IEEE Trans. Image Process.*, vol. 27, no. 8, pp. 4118–4130, Aug. 2018.
[42] A. Cichocki, D. P. Mandic, L. D. Lathauwer, G. Zhou, Q. Zhao, C. F. Caiafa, and H. A. Phan, "Tensor decompositions for signal processing applications: From two-way to multiway component analysis" *IEEE Signal Process. Mag.*, vol. 32, no. 2, pp. 145–163, Mar. 2015.
[43] L. D. Lathauwer, "Decompositions of a higher-order tensor in block termspart II: Definitions and uniqueness" *SIAM J. Matrix Anal. Appl.*, vol. 30, no. 3, pp. 1033–1066, Jan. 2008.
[44] S. Boyd, N. Parikh, E. Chu, B. Peleato, and J. Eckstein, "Distributed optimization and statistical learning via the alternating direction method of multipliers" *Found. Trends Mach. Learn*, vol. 3, no. 1, pp. 1–122, 2010.
[45] Y. Qu and H. Qi, "uDAS: An untied denoising autoencoder with sparsity for spectral unmixing" *IEEE Trans. Geosci. Remote Sens.*, vol. 57, no. 3, pp. 1698–1712, Mar. 2019.

Heng-Chao Li (Senior Member, IEEE) received the B.Sc. and M.Sc. degrees from Southwest Jiaotong University, Chengdu, China, in 2001 and 2004, respectively, and the Ph.D. degree from the Graduate University of Chinese Academy of Sciences, Beijing, China, in 2008, all in information and communication engineering.

He is currently a Full Professor with the School of Information Science and Technology, Southwest Jiaotong University. From November 2013 to October 2014, he has been a Visiting Scholar working with Prof. W. J. Emery with the University of Colorado Boulder, Boulder, CO, USA. He has authored more than 100 research papers, including 65 JCR journal papers, such as published in the ISPRS *Journal of Photogrammetry Remote Sensing*, IEEE TRANSACTIONS ON GEOSCIENCE AND REMOTE SENSING, the IEEE JOURNAL OF SELECTED TOPICS IN SIGNAL PROCESSING, IEEE TRANSACTIONS ON IMAGE PROCESSING, and the *Pattern Recognition*. His research interests include statistical analysis of SAR images, remote sensing image processing, and pattern recognition.

Prof. Li was a recipient of the 2018 Best Reviewer Award from IEEE Geoscience Remote Sensing Society for his service to the IEEE JOURNAL OF SELECTED TOPICS IN APPLIED EARTH OBSERVATIONS AND REMOTE SENSING Remote SENSING (JSTARS). He is currently serving as an Associate Editor for the IEEE JSTARS, and is an Editorial Board Member of the *Journal of Southwest Jiaotong University and the Journal of Radars*. Moreover, he has served as a Guest Editor of Special Issues of the *Journal of Real-Time Image Processing*, the IEEE JSTARS, and the IEEE JMASS, a Program Committee Member for the 26th International Joint Conference on Artificial Intelligence (IJCAI-2107) and the 10th International Workshop on the Analysis of Multitemporal Remote Sensing Images (MULTITEMP-2019), and the Session Chair for the 2017 International Geoscience Remote Sensing Symposium (IGARSS-2017) and the 2019 Asia-Pacific Conference on Synthetic Aperture Radar (APSAR-2019). He is also an Active Reviewer of more than 30 international journals.

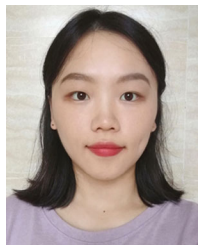

Shuang Liu received the B.Sc. degree in communication engineering from the Southwest Jiaotong University, Chengdu, China, in 2018. She is currently working toward the M.Sc. degree in computer science and technology with the School of Information Science and Technology, Southwest Jiaotong University, Chengdu, China.

Her research interests include hyperspectral image analysis and processing.

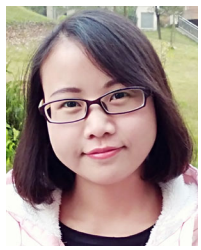

Xin-Ru Feng received the B.Sc. degree in communication engineering from the Southwest Jiaotong University, Chengdu, China, in 2016. She is currently working toward the Ph.D. degree in signal and information processing with the School of Information Science and Technology, Southwest Jiaotong University, Chengdu, China.

Her research interests include hyperspectral image analysis and processing.

Shao-Quan Zhang received the B.S. and M.E. degrees from Nanchang Institute of Technology, Nanchang, China, in 2012 and 2015, respectively, and the Ph.D. degree from the Sun Yat-sen University, Guangzhou, China, in 2018.

He is currently a Lecturer with Jiangxi Province Key Laboratory of Water Information Cooperative Sensing and Intelligent Processing, Nanchang Institute of Technology, Nanchang, China. His research interests include hyperspectral unmixing, sparse representation, and machine learning.